# Electron channelling contrast imaging for III-nitride thin film structures

G. Naresh-Kumar*, D. Thomson, M. Nouf-Allehiani, J. Bruckbauer, P. R. Edwards, B. Hourahine, R. W Martin and C. Trager-Cowan

Department of Physics, SUPA, University of Strathclyde, Glasgow G4 0NG, UK

* E-mail: naresh.gunasekar@strath.ac.uk

**Keywords:** ECCI, III-nitrides, extended defects, SEM and thin films.

**Abstract:**

Electron channelling contrast imaging (ECCI) performed in a scanning electron microscope (SEM) is a rapid and non-destructive structural characterisation technique for imaging, identifying and quantifying extended defects in crystalline materials. In this review, we will demonstrate the application of ECCI to the characterisation of III-nitride semiconductor thin films grown on different substrates and with different crystal orientations. We will briefly describe the history and the theory behind electron channelling and the experimental setup and conditions required to perform ECCI. We will discuss the advantages of using ECCI; especially in combination with other SEM based techniques, such as cathodoluminescence imaging. The challenges in using ECCI are also briefly discussed.

## 1. Introduction:

III-nitrides are the only class of commercially available inorganic semiconducting materials with the potential to emit light from the infrared to the ultraviolet (with commercial devices available in the green to the ultraviolet part of the spectrum) with direct band gaps ranging from 0.7eV for InN to 6.2eV for AlN [1]. In the last 25 years, the development of a wide variety of nitride–based photonic and electronic devices has opened a new epoch in the field of semiconductor research. Nitride semiconductors are used in light emitters, photodiodes and high–speed/high–power electronic devices [2, 3]. For these reasons nitride semiconductors have attracted much attention from both the consumer product industries and the defence sector, engendering intensive research with the aim of improving device efficiencies and reducing their costs.

One method for improving the performance of nitride–based devices is the reduction of the polar and piezoelectric fields which are a result of the wurtzite crystal structure and strain induced in device structures, respectively. This can be achieved by growing on nonpolar, m-plane (1-100) and a-plane (11-20), or semipolar, (11-22) and (20-21), planes. Growth of semipolar InGaN/GaN quantum well structures also enables the effective incorporation of higher concentrations of InN [4], improving the efficiency of amber and red nitride based light emitting diodes (LEDs).

A range of crystal growth technologies is being developed for the realisation of GaN substrates with large size (2 to 6 inch) and high quality, especially for the polar (0001) c-plane GaN [5]. However, the sizes of nonpolar and semipolar GaN substrates remain small and their cost is too high [6-8].

Heteroepitaxial growth on sapphire and silicon substrates is cheaper than growth on bulk GaN. However, heteroepitaxially grown nitrides suffer from a high density of extended defects such as threading dislocations (TDs), basal plane stacking faults (BSFs) and

associated partial dislocations (PDs) mainly due to the large lattice mismatch between the heteroepitaxial substrate and the epilayer [9]. In addition to lattice mismatch, differences in thermal expansion coefficients cause biaxial stress to the epitaxial layer; for example GaN is compressively strained when c-plane sapphire is used as a substrate material [10]. Irrespective of the substrates, growth plane or growth techniques employed, extended defects are always present in the as-grown layers and have proven to be detrimental to device performance [11-14]. In order to optimise the growth and thereby improving the crystal quality, we require a rapid, non-destructive and cost-effective structural characterisation technique for detailed understanding of extended defects and their formation.

Recent advancements have made x-ray diffraction (XRD) a powerful tool for characterising nitride semiconductors, but there are several limitations, especially in using XRD to characterise non-polar nitrides [15]. Modified Williamson-Hall analysis is a widely used method to estimate stacking fault densities in nonpolar GaN thin films [16]. However, the accuracy of this technique is limited to line densities above $10^4 cm^{-1}$. Moreover, the applicability of this method is questionable as other superimposing effects, such as surface morphology and wafer bowing, may produce unphysical results [17]. At present, transmission electron microscopy (TEM) is the best known and most widely used technique for characterising individual threading dislocations and stacking faults [18-20] in nitride semiconductors. The need for sample preparation and the localised nature of the information acquired from TEM make other microscopic imaging techniques such as atomic force microscopy (AFM) – and the subject of this review, electron channeling contrast imaging (ECCI) – attractive complementary techniques to TEM.

We will begin this review by providing a brief history of electron channelling followed by theoretical and practical aspects of the technique. Through results from a wide range of nitride thin films grown by metalorganic vapour phase epitaxy (MOVPE), we will

illustrate that ECCI can be used to reveal (i) individual dislocations, (ii) atomic steps, (iii) low angle tilt and rotation boundaries (iv) basal plane stacking faults and associated partial dislocations. We will also show that the range of magnifications and resolution afforded by ECCI in the SEM allows dislocation densities to be measured over a wide range of densities. The large field of view also allows the distribution of dislocations to be studied, for example we have observed long range ordering as well as clustering of dislocations. We will also discuss the advantages of using ECCI with other techniques in the SEM; especially in combination with cathodoluminescence (CL) imaging. Finally we will summarise our results and discuss a few remaining challenges to using ECCI for characterising nitride semiconductor thin films.

### 1.1 Brief history of ECCI.

The first observation of dislocation networks in thin foils of aluminium and copper recorded with backscattered electrons (BSEs) in a scanning electron microscope (SEM) was performed by Clarke in 1971 [21] followed by Stern and Kimoto in 1972 (imaging dislocations in molybdenite) [22]. The importance of using a field emission gun scanning electron microscope (FEG–SEM) was realised from their work and the first observation of dislocations (also in molybdenite) using a FEG–SEM was obtained by Pitaval et al in 1976 [23-25]. The term ECCI was first used by Morin et al in 1979 [26] who were able to image extended defects in semiconductors (Si) using ECCI. Seminal work from Joy and Newbury et al for characterising metals [27], Wilkinson et al in imaging misfit dislocations in $Si_{1-x}Ge_x$ thin films, and improvement in detector geometries opened up the possibilities of using ECCI for variety of materials [28,29]. Trager–Cowan and co–workers [30] were the first to apply ECCI to the imaging of threading dislocations in nitride semiconductors followed by Picard et al [31] who used ECCI to investigate SiC [32], and $SrTiO_3$ [33]. Recently Carnevale and

co-workers used ECCI to image misfit dislocations in GaP [34] and Yan et al applied the technique to image antiphase domains boundaries in $LaSrMnO_3$ thin films [35]. Some of our own work [36-40] and recent work from our collaborators [41-43] have taken ECCI a step further as a quantitative technique for characterising nitride semiconductor thin films by resolving individual dislocation types over statistically significant dislocation distributions, opening up new possibilities for advanced materials characterisation.

### 1.2 Principle of electron channelling.

Contrast from electron channelling can be used in two modes of operation [44, 45]. The first of these is the acquisition of electron channelling patterns (ECPs) which allows the selection of the set of planes from which the electrons are diffracted. This procedure is referred to as selecting a diffraction vector, **g**. This is analogous to choosing diffraction conditions in TEM. Detailed description of ECPs is beyond the scope of this review, more information on this topic can be found in the references [27, 44, and 45]. The second mode of operation is obtaining ECC images, the main focus of this review. When the SEM is operated at a very high magnification, the angle between the scanned beam and the surface remains constant. As a result, changes in crystallographic orientation or changes in lattice constant due to local strain are revealed by changes in contrast in a channelling image constructed by monitoring the intensity of BSE as an electron beam is scanned over the suitably oriented sample. Images with resolution of the order of tens of nanometres can be obtained by ECCI. Extremely small changes in orientation ($\approx 0.01^{\circ}$) [42] and strain are detectable, revealing for example low angle tilt and rotation boundaries and atomic steps and enabling extended defects to be imaged.

The conditions required to resolve individual dislocations in an ECC image are quite stringent: a small (nanometres), high brightness (nanoamps or higher), low divergence or

high convergence beam (of order of a few mrad) electron beam is required [46, 47]. These conditions are necessary to obtain good quality channelling contrast and they are met only in a field emission SEM (FEG–SEM). All the ECC images in the present work were acquired using an FEI Sirion 200 Schottky FEG–SEM with an electron beam spot of ≈ 4 nm, a beam current of ≈ 2.5 nA and a beam divergence of ≈ 4 mrad. It is also necessary to use a detection system that allows discrimination between those electrons leaving the sample which carry channelling information and those which have been diffusely scattered by the sample. An amplifier which can offset the diffuse background signal and a preamplifier to amplify the channelling signal is required. In the present work, the forescatter Si diodes, preamplifier and a signal amplifier were provided by KE Developments Ltd, now Deben, UK.

ECC images can be acquired in either forescatter geometry (sample tilted to between 30° and 70° to the impinging electron beam and the forescatterd electrons detected by a diode placed in front of the sample) [30] or the backscatter geometry (sample at approximately 90° degrees to the incident electron beam with the BSE detected by an electron–sensitive diode or diodes placed on the pole piece of the microscope) [48]. Figures 1a and 1b show the schematic of forescatter and the backscatter geometries respectively and1c and 1d show the corresponding ECCI respectively .The ECC image shown in figure 1 c is acquired by tilting to sample to 70˚ whereas the ECC image shown in figure 1 d is acquired with sample approximately flat (not tilted). Note the images are not from the same part of the sample. The acquisition time required to obtain each image is typically less than a minute.

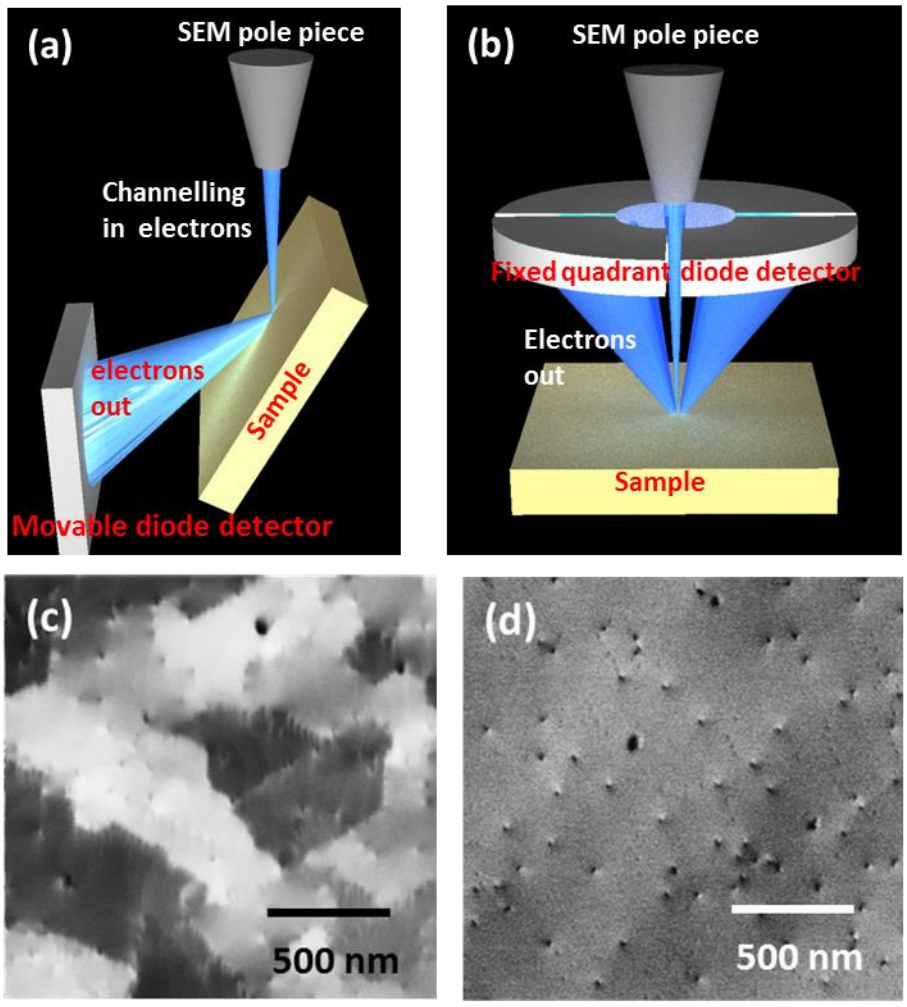


**Figure 1: (a) Experimental geometry used in the present work (forescatter geometry), (b) backscattered geometry, (c) ECCI in forescatter and (d) backscattered geometry from a GaN capped AlGaN/GaN HEMT structure grown on Si. Note the ECC images are not from the same area.**

The backscatter geometry has the advantage that large samples, e.g., a full semiconductor wafer (depending on the size of the SEM chamber), could be imaged and the results obtained may be more easily compared to a TEM diffraction image. The forescatter geometry requires tilt correction of the acquired images but provides a larger channelling signal and therefore channelling images with superior signal to noise. The forescatter geometry is the one used in our present work.

## 2. Results and discussion:

### 2.1 ECCI of GaN thin films

In ECCI, vertical threading dislocations appear as spots with black–white (B–W) contrast; this is shown in Fig. 2 a, an ECC image acquired from a 1600 nm thick GaN thin film grown on a sapphire substrate in which a typical threading dislocation is highlighted by a black circle [49]. The (B-W) contrast is basically due to strain fields around a dislocation. For materials with a wurtzite crystal structure such as GaN, we have previously developed a simple geometric procedure to identify a given threading dislocation as edge, screw, or mixed type by exploiting differences in the direction of the black–white contrast between two ECC images acquired under 2–beam conditions from two symmetrically equivalent crystal planes whose diffraction vector (**g**) are at 120° to each other, where the **g**-vector was determined through the acquisition of ECPs [37]. To identify the dislocation types we monitor the changes in the direction of the B-W contrast that occur when the **g**-vector is changed. The B-W contrast direction is perpendicular to **g** for a pure screw dislocation, whereas for an edge dislocation the direction of the B-W contrast depends on its Burgers vector and not on **g**. Hence for edge dislocations, we expect the direction of B-W to either reverse or remain the same when the diffraction conditions are changed. Mixed dislocations may be identified as their B-W contrast direction changes in a manner intermediate to that of the edge and screw dislocations. In practice it is difficult to achieve exact 2–beam conditions; however it is possible to get sufficiently close to allow quantitative analysis of the resultant ECC images. In general, ECC images are always acquired under multi-beam conditions as they exhibit better signal to noise than those obtained using 2–beam conditions. All the images shown in the present work were acquired under multi-beam conditions to allow an estimation of the total threading dislocation density.

From a series of images such as that shown in Fig. 2 a, the total dislocation density for the 1600 nm thick GaN thin film grown on a sapphire substrate was determined to be $3.5 \times 10^8$ cm$^{-2}$. Through a detailed analysis of ECC images acquired under selected two beam conditions as described above [37] (not shown here), the percentage of pure edge dislocations for this sample was found to be ≈ 51%, followed by mixed at ≈ 42%. Pure screw dislocations accounted for only ≈ 7% of the total threading dislocation density. The ratio of the types of individual dislocations depends on the growth conditions and in general screw dislocations are fewer in number when compared to the mixed and edge due to the higher formation energy needed to make them stable. For this sample, the relative densities of screw to edge are of the same order (7.3:1 as compared to 5.3:1) to those estimated from X–ray diffraction measurements [49]. In addition to imaging threading dislocations, it is also possible to image atomic steps (see figure 2a) revealing the step flow growth mode, typical in MOVPE growth of nitride thin films.

### 2.2 ECCI of HEMT and DBR structures

ECCI also reveals low angle tilt and rotation boundaries. This is illustrated in figure 2b which shows an ECC image from a 5 nm GaN capped AlGaN/GaN high electron mobility transistor (HEMT) structure grown on a Si (111) substrate [50]. Two different grains with different tilt/rotation marked as grain A (dark contrast) and grain B (bright contrast) can be clearly seen in figure 2b. On changing the diffraction conditions, it is possible to change the contrast of the subgrains from being bright to being dark as demonstrated in our previous work [37]. However, just from ECC images, it is not straightforward to quantify the misorientations of the grains [51], but this can be achieved by combining ECCI with electron backscatter diffraction (EBSD) [42]. The total threading dislocation density estimated for this

sample is found to be $5 \times 10^9$ $cm^{-2}$, nearly an order of magnitude higher than for the1600 nm GaN on sapphire sample.

Care has to be taken in estimating the threading dislocation density as different samples exhibit different defect distributions, ranging from completely random to clustered behaviour [52]. It is also possible to have different distribution of threading dislocations from different areas within a single sample grown on large substrates (example: GaN on 6 inch Si). For such samples, it is advisable to acquire ECC images over a range of magnifications to estimate a statistically significant threading dislocation density. This approach can be time consuming, however in practise at least three ECC images from different scan areas where individual dislocations can be resolved are generally used to estimate the total threading dislocation density.

Performing ECCI in the forescatter geometry is also useful in enhancing the surface topography as shown by the dotted black rectangle in figure 2c, which shows the honeycomb/hillock surface morphology usually seen in MOVPE grown InAlN surfaces [53]. The ECC image in figure 2c is from a 3 nm thick InAlN/AlN/GaN HEMT structure grown on 4H-SiC substrate. SiC has a smaller lattice mismatch and more suited to grow HEMT structures due to the availability of highly insulating SiC substrates of good crystal quality. The threading dislocation density for this sample is estimated to be $6 \times 10^7$ $cm^{-2}$. Growth conditions on similar sample structures can be found elsewhere [40].

The quality of the epitaxial layer mainly depends on the substrate/surface it is grown on as well as on the growth conditions. Figure 2d shows an ECC image from $In_{0.20}Al_{0.80}N$/GaN bilayers (42 pairs) which make up a distributed Bragg reflector structure grown on a free standing GaN thin film [54]. As can be clearly seen from figure 2d, fewer dislocations (a TD density of $4 \times 10^7$ $cm^{-2}$) are found in this sample when compared to the ECC images showed in figure 2a and 2b. This is due to the good crystal quality attained by

homo-epitaxial growth of InAlN/GaN bilayers on free standing GaN substrates. Thus it is possible to characterise threading dislocations from nitride thin films grown on different substrates and exhibiting varying defect densities.

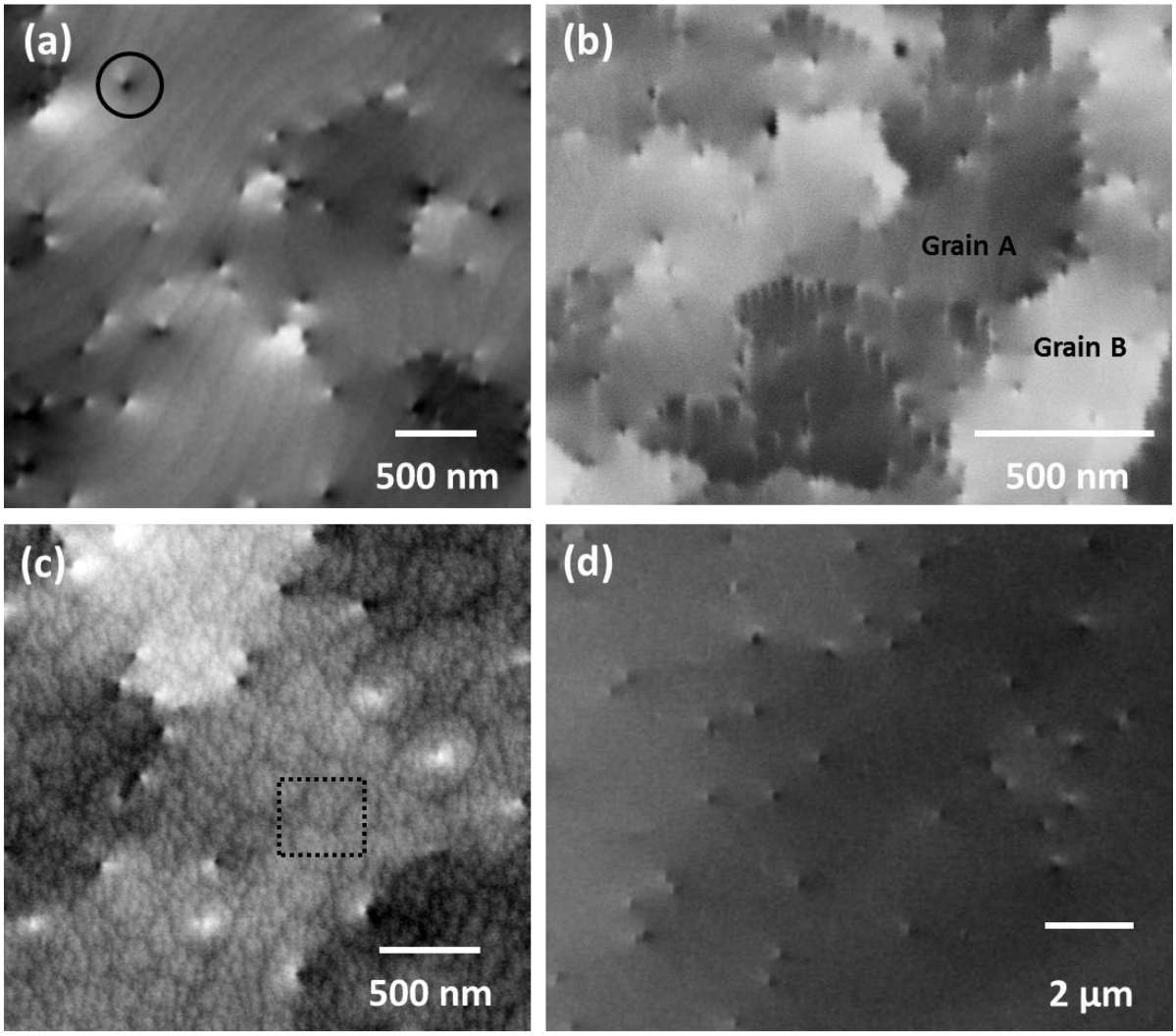


**Figure 2: Electron channeling images of (a) 1.6 µm GaN film grown on sapphire, (b) 5 nm GaN layer on top of AlGaN/GaN HEMT structure grown on Si, (c) 3 nm InAlN/Aln/GaN HEMT structure grown on 4-H SiC and (d) InAlN/GaN DBR grown on a free standing GaN substrate.**

### 2.3 ECCI of nonpolar and semipolar GaN.

In addition to imaging threading dislocations, ECCI can also be used to image stacking faults in nitride thin films [38]. Figure 3a shows an ECC image from an m-plane (1-100) GaN buffer layer of 900 nm grown on top of a (100) γ–$LiAlO_2$ substrate revealing a striated pattern along [0001] [55-57]. The striations are related to the anisotropic growth mode of m-plane GaN on $LiAlO_2$ [55]. A basal plane stacking fault in ECCI appear as a line with a partial dislocation terminating each end. The contrast mechanism for basal plane stacking fault is similar to threading dislocations as both of them strain the crystal lattice. Basal plane stacking faults can appear as a line with B–W contrast as shown in the dotted white box in figure 3a in which the basal plane stacking fault is running along the [11-20]. They can also appear just as a black or white line depending on the diffraction conditions. Previous TEM investigations on this sample show the observed basal plane stacking faults to be of $I_1$ type [38]. Note the majority of the observed stacking faults in nitrides are of $I_1$ type. However other types such as $I_2$, $I_3$, prismatic and extrinsic stacking faults are also found in nitride thin films [58].

Additional care has to be taken when counting stacking faults to build up statistically significant values for estimating their densities. Stacking fault densities are typically represented as line densities ($cm^{-1}$) which are calculated by dividing the stacking fault area by the probed volume of the sample. In TEM, basal plane stacking fault densities can be measured from plan view and/or cross–sectional images, whereas in our present ECCI, the basal plane stacking fault densities are estimated solely from plan view images. As ECCI can yield information from a larger field of view, up to of order 500 $\mu m^2$, statistically significant numbers for defect densities can be estimated. In the present work, threading dislocation, basal plane stacking fault and partial dislocation densities were estimated from several images each with an area of ≈ 5 $\mu m^2$, The threading dislocation density for the m-plane GaN

buffer layer was found to be $2 \times 10^9$ $cm^{-2}$. Assuming the basal plane stacking faults propagate through the entire sample, their line density was estimated to be $\approx 0.6 \times 10^4$ $cm^{-1}$. In order to increase the reliability of the analysis without any assumptions, basal plane stacking fault number densities (area densities) [59] were also estimated by simply counting the total number of basal plane stacking faults appearing in the entire field of view in the ECCI images. For the m-plane GaN buffer layer, the basal plane stacking fault number density was found to be $9 \times 10^7$ $cm^{-2}$ with a corresponding partial dislocation density of $2 \times 10^8$ $cm^{-2}$. This is an order of magnitude lower than the threading dislocation density. Figure 3b shows the ECCI from a 6 μm thick a-plane (11-20) GaN grown on a r-plane sapphire substrate using onside epitaxial lateral over growth technique [60]. Due to the nature of growth, the distribution of threading dislocations is not random in this case. This can be seen by the line of dislocations (see marked white rectangle). The threading dislocation density for this sample was found to be $8 \times 10^8$ $cm^{-2}$.

Semipolar GaN and their alloys have attracted recent interest and eliminating extend defects in these structures is currently a hot research topic [61]. The ECC image shown in figure 3b is from a 5 μm thick semipolar (11-22) GaN layer grown on m-plane sapphire [62]. In addition to clustering of threading dislocations as highlighted by the black dotted rectangle in figure 3b, arrow head shaped features also known as chevrons are seen on the sample surface [61]. Clustering of dislocations occurs during growth. For example lines of dislocations, such as those observed in Fig.3b are often observed. It has been shown that edge TDs may move during growth following coalescence, forming stable low-energy lines of dislocations aligned along preferential directions [52].The total threading dislocation density for this sample is estimated to be $1 \times 10^9$ $cm^{-2}$. The topographic features due to the surface morphology, dominate the diffraction contrast for our measurement geometry. However, by careful

selection of detector placement and diffraction conditions, the diffraction contrast can be enhanced.

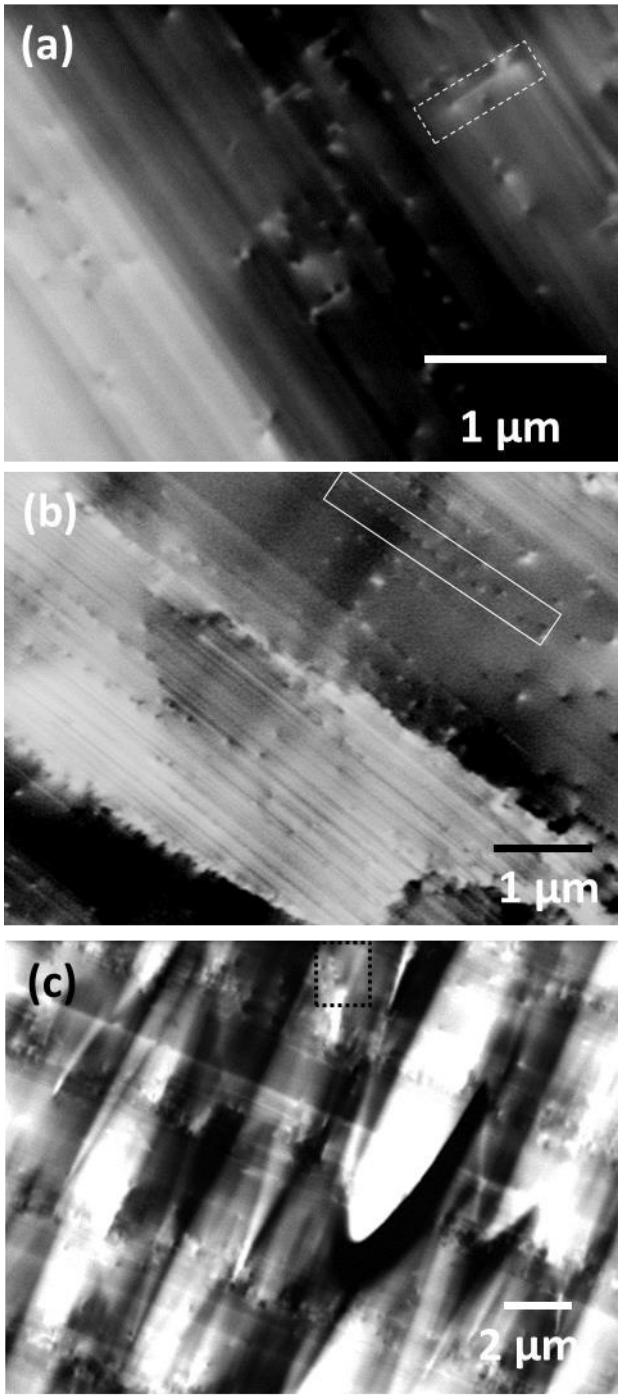


**Figure 3: (a) Electron channelling images of (a) m-plane GaN grown on lithium aluminate a-plane GaN grown on lithium aluminate and (c) semipolar (11-22) GaN grown on m-plane sapphire**.

### 2.4 Combining ECCI with CL imaging and other SEM related techniques

ECCI being an SEM based technique; makes it relatively easy to combine with other SEM based techniques such as EBSD [42] and CL hyperspectral imaging [39]. Combining ECCI with CL imaging is ideal for understanding the effect of extended defects on the optical properties of nitride semiconductors, for example to ascertain if all types of threading dislocations act as non–radiative recombination centers. Figure 4 shows an ECCI and room temperature CL intensity image of the GaN near band edge emission peak acquired from exactly the same micron–scale area of a Si-doped GaN thin film grown on a sapphire substrate [39]. Cathodoluminescence imaging was performed with an electron beam spot size of ≈ 17 nm, a beam current of ≈ 6 nA and accelerating voltage of 5 keV. Both the images were aligned to match the same area due to the difference in geometries involved in ECCI and cathodoluminescence imaging. Figure 4 shows only a small area of the original data in order to clearly discern the individual dislocations. The original data set is of ≈ 150 $\mu m^2$ in area with ≈ 750 dislocations of which ≈ 400 dislocations were found to be isolated while the remaining are clustered (more than two dislocations near to each other). It is advisable to perform ECCI measurements before cathodoluminescence imaging to avoid any surface contamination which can reduce the clarity of channelling images. More information on CL imaging for nitrides can be found in the references [63-65]. For the ECC image showed in figure 4a, it is possible to discriminate between threading dislocations which are further than ≈ 80 nm apart. The average threading dislocation density for the sample was estimated to be $5 \times 10^8$ $cm^{-2}$, calculated by averaging the dislocation count from a number of ECC images. Some of the threading dislocations (of order 5% in the ECC image, such as the one highlighted by a solid white circle), are observed to have fainter and elongated contrast, that is, appearing as short lines ≈100 nm in length. We surmise that these are projections of inclined threading dislocations (dislocations are observed to bend in Si-doped GaN [66]). The

corresponding dark spot for the inclined dislocation is showed as dotted white circle in the CL image. For the CL map shown in figure 4b, dark spots corresponding to single, isolated threading dislocations have a diameter of ≈150 nm. In this case the size of the dark spots in the CL is mostly defined by the size of the excitation volume and not the carrier diffusion length. A comparison of both images shows a one–to–one correlation for isolated threading dislocations in ECCI with dark spots in CL imaging. The regions of the sample showing highest CL intensity appear to coincide with regions of the sample free of dislocations. However, not all dislocation-free regions show bright CL, possibly indicating the presence of other defects such as point defects. In regions containing clusters of threading dislocations, it was not possible to unambiguously determine if all the dislocations in the clusters correspond to the larger dark spots in the CL image. AFM images were also acquired from the same part of the sample (images not shown here) revealing that isolated dislocations are of both edge and screw/mixed character. Thus one may come to the conclusion that pure edge dislocations and dislocations with screw component appear to act as non–radiative recombination centers for the analysed sample.

In addition to combining ECCI with cathodoluminescence and EBSD, It also possible to perform ECCI and electron beam induced current (EBIC) from the same area, however sample preparation is needed especially in making electrical contacts for the EBIC measurements. In theory it is also possible to perform ECCI and X - ray microanalysis (EXD/WDX) together in the same instrument.

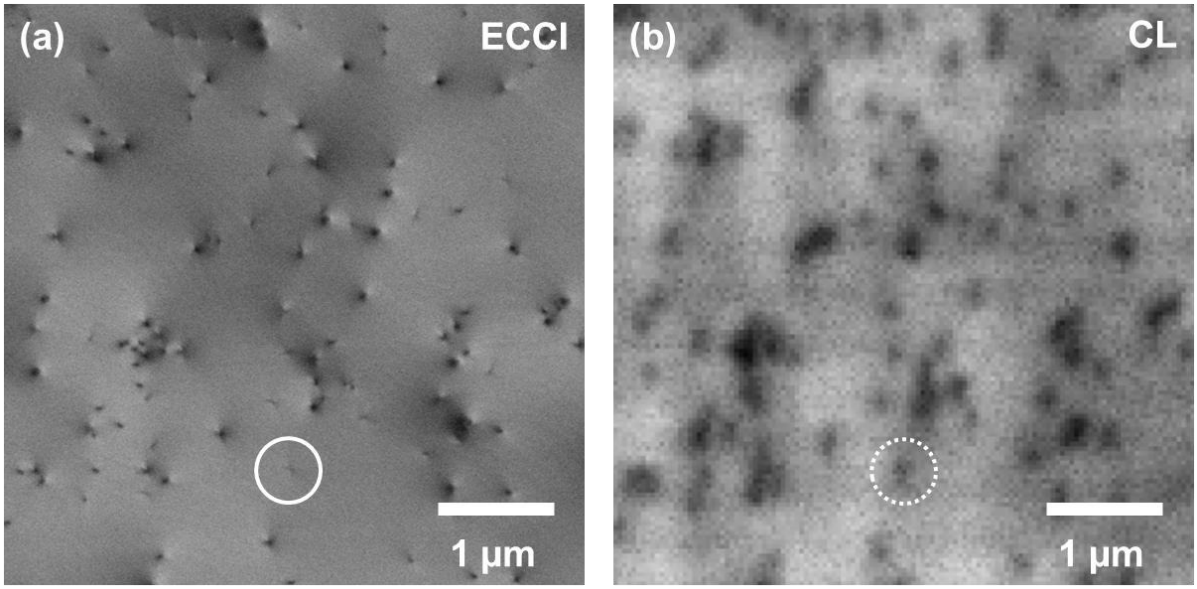


**Figure 6: (a) Electron channeling image and (b) CL intensity image of the GaN band edge emission peak from the same micron–scale area. Threading dislocations appearing as spot with B–W contrast in ECCI appear as dark spots in CL revealing a direct correlation of threading dislocations between both techniques.**

### 2.5 Present challenges with ECCI.

No characterisation technique is without challenges, and ECCI is no exception. The requirement to know the diffraction conditions necessitates the acquisition of ECPs, without which differentiating between a pure screw and a mixed dislocation is not possible in nitride semiconductors. Although for most nitride semiconductors the sample surface is smooth enough to allow the imaging of threading dislocations by ECCI, only a few samples are of good enough crystal quality to allow the acquisition of ECPs. If good quality sample surfaces are available, reasonable sample size (of the order of 1 × 1 cm) is required to acquire ECPs without any additional electron optics. However, recent developments in acquiring ECPs from small areas (of the order of tens of µm) by rocking the beam appear to be a promising

solution [67]. Although it is possible to acquire AFM-like images revealing topography and atomic steps and imaging sub-grains, ECCI is not yet a reliable quantitative method for surface topography and misorientation analysis. Recent developments in combining ECCI with EBSD [42] and AFM [39] may offer a route forward to address this problem. It is still not clear from what depth in the sample the diffracted information is coming from. It is widely believed to be from tens of nanometres; however, it is yet to be confirmed by advanced electron diffraction calculations. Recent work from De Graef [68] and Picard et al [69] shows progress in detailed theoretical understanding of ECCI.

## 3 Summary and conclusion:

The present work provides a comprehensive demonstration of ECCI for characterising nitride semiconductor thin films. We have shown examples from GaN thin films and their alloys grown on different substrates and with different orientations. The obtained images are similar to plan view TEM style images with lower resolution (tens of nanometres as opposed to sub-nanometre) when compared to TEM. However, high quality images can be acquired under multibeam conditions and quantitative analysis of extended defects can be performed under known diffraction conditions with the help of ECPs. In addition to choosing appropriate diffraction conditions, optimum incident electron beam conditions and backscattered electron detection conditions have to be fulfilled to acquire ECCI with high contrast/ intensity. We have demonstrated ECCI as a rapid, non-destructive and cost-effective structural characterisation technique for detailed understanding of extended defects in nitride semiconductor thin films. Combining ECCI with other SEM based technique such as CL imaging can be beneficial in understanding the influence of extended defects on the optical properties of nitride semiconductors.

**Acknowledgements:**

We would like to thank all our growth colleagues for providing samples for our ECCI characterisation work at the University of Strathclyde. Special thanks to Prof. Peter Parbrook, University College Cork, Ireland, Dr Rachel Oliver, University of Cambridge, Dr Trevor Martin, IQE, UK and Dr Christof Mauder and Prof. Michael Heuken, Aixtron SE, Germany for providing variety of GaN samples. We are grateful to Prof. Tao Wang, University of Sheffield for providing semipolar GaN thin films. We would also like to thank Dr M. A. di Forte-Poisson and Dr Piero Gamarra, Thales Research and Technology, France for providing HEMT structures and Prof. Nicolas Grandjean, EPFL, Switzerland for providing DBR structures. This work was supported by the EU project no. PITN–GA–2008–213238 (RAINBOW) and the EPSRC project EP/J015792/1.

**References:**

1. F. Schubert, Light–emitting diodes, Cambridge University press, London (2003).

2. S. P. DenBaars, Introduction to Nitride Semiconductor Blue Lasers and Light Emitting Diodes, CRC press, Newyork (2000).

3. H. Morkoc, Handbook of Nitride Semiconductors and Devices, Wiley-VCH, Germany (2008).

4. T. Wernicke et al Semicond. Sci. Technol. **27, 024014** (2012).

5. T. Paskova, D. A. Hanser and K. R. Evans P.IEEE **98**, 1324 (2010).

6. Fujito K, Kubo S, Nagaoka H, Mochizuki T, Namita H and Nagao S. , J. Cryst. Growth **311,** 3011 (2009).

7. Hashimoto T, Wu F, Speck J S and Nakamura S., Nat.Mater. **6,** 568 (2007).

8. Dwiliński R, Doradziński R, Garczyński J, Sierzputowski L P, Puchalski A, Kanbara Y, Yagi K, Minakuchi H and Hayashi H., J. Cryst. Growth **310,** 3911 (2008).

9. M. F. Schubert, S. Chhajed, J. K. Kim, and E. F. Schubert, Appl. Phys. Lett. **91**, 231114 (2007).

10. T. Kozawa, T. Kachi, H. Kano, H. Nagase, N. Koide, and K. Manabe, J. Appl. Phys. **77**, 4389 (1995).

11. S. Nakamura, Science, **281**, 956 (1998).

12. D. C. Look and J. R. Sizelove, Phys. Rev. Lett. **82**, 1237 (1999).
13. K. H. Baik, Y. G. Seo, S. Hong, S. Lee, J. Kim, J. Son, and S. Hwang, IEEE Photon. Technol. Lett. **22**, 595 (2010).
14. J. Kioseoglou, E. Kalesaki, L. Lymperakis, J. Neugebauer, Ph. Komninou, and Th. Karakostas, J. Appl. Phys. **109**, 083511 (2011).
15. V. M. Kaganer, O. Brandt, A. Trampert, and K. H. Ploog, Phys. Rev. B **72**, 045423 (2005).
16. M. B. McLaurin, A. Hirai, E. Young, F. Wu, and J. Speck, Jpn. J. Appl. Phys., **47**, 5429 (2008).
17. M. A. Moram, C. F. Johnston, J. L. Hollander, M. J. Kappers, and C. J. Humphreys, J. Appl. Phys. **105**, 113501 (2009).
18. D. M. Follstaedt, N. A. Missert, D. D. Koleske, C. C. Mitchell, and K. C. Cross, Appl. Phys. Lett. **83**, 4797 (2003).
19. R. Datta, M. J. Kappers, J. S. Barnard, and C. J. Humphreys, Appl. Phys. Lett. **85**, 3411 (2004).
20. F. Wu, Y. D. Lin, A. Chakraborty, H. Ohta, S. P. DenBaars, S. Nakamura, and J. S. Speck, Appl. Phys. Lett. **96**, 231912 (2010).
21. D. R. Clarke, Phil. Mag., **24,** 973, (1971).
22. R**.** M Stern, T. Ichinochawa, S. Takashima, H. Hashimoto, and S. Kimoto, Phil. Mag., **26**, 1495 (1972).
23. M. Pitaval, P. Morin, J. Baudry and G. Fontaine, Emag., **75**, 20 (1975).
24. M. Pitaval, P. Morin, J. Baudry and G. Fontaine, Microsc. Spectrosc. Electron., **2**, 185 (1977).
25. M. Pitaval, P. Morin, J. Baudry, G. Fontaine and E. Vicario, Scanning Electron Microscopy, **1**, 439, (1977).
26. P. Morin, M. Pitaval, D. Besnard and G. Fontaine, Phil. Mag. A, **4**, 511(1979).
27. D. C. Joy, D. E. Newbury and D. L. Davidson, J. Appl. Phys. **53**, 81 (1982).
28. A. J. Wilkinson, G. R. Anstis, J. T. Czernuszka, N. J. Long and P. B. Hirsch, Phil. Mag. A **68**, 59 (1993).
29. A. J. Wilkinson and P. B. Hirsch, Micron **28**, 279 (1997).
30. C. Trager-Cowan. et al., Phy. Rev. B **75**, 085301 (2007).
31. Y. N. Picard et al., Scripta Materialia **61**, 773 (2009).
32. Y. N. Picard and M. E. Twigg, J. Appl. Phys. **104**, 124906 (2008).
33. R. J. Kamaladasa , W. Jiang, Y. Picard Journal of Elec. Mat., **40**, 11 (2011).

34. S. D. Carnevale et al Appl. Phys. Lett. **107**, 041601 (2015).
35. Miaolei Yan, Marc De Graef, Yoosuf N. Picard and Paul A. Salvador Appl. Phys. Lett. 107, 041601 (2015).
36. G. Naresh-Kumar et al, Phys. Status Solidi A, **209**, 424 (2012).
37. G. Naresh-Kumar et al, Phys. Rev. Lett., **108**, 135503 (2012).
38. G. Naresh-Kumar et al, Appl Phys Lett., **102**, 142103 (2013).
39. G. Naresh-Kumar et al, Microsc. Microanal., **20**, 55 (2014).
40. G. Naresh-Kumar et al, AIP Advances, **4**, 127101 (2014).
41. S. Nagarajan et al, Appl Phys Lett., **103**, 012102 (2013).
42. Arantxa et al Microsc. Microanal. **21** (Suppl 3), 2015
43. E.V. Lutsenko et al, Journal of Crystal Growth, **434**, 62 (2016).
44. D. B. Holt and D. C. Joy, SEM microcharacterization of semiconductors, academic press, London (1989).
45. J. I. Goldstein et al., Scanning Electron Microscopy and X-ray microanalysis, Plenum press, New York (1981).
46. A. P. Laponsky and N. R. Whetten Phys. Rev. Lett., **3**, 510 (1959).
47. J. P. Spencer, C. J. Humphreys and P. B. Hirsch, Phil. Mag., **26**, 193 (1972).
48. B. A. Simpkin and M. A. Crimp, Ultramicroscopy, **77**, 65 (1999).
49. T. A. Lafford, P. J. Parbrook, and B. K. Tanner, phys. stat. sol. c **1**, 542 (2002).
50. D. Thomson et al "ECCI of AlGaN/GaN HEMT structure grown on Si", UKNC meeting January 2015.
51. A P. Day T. E. Quested, Journal of Microscopy,**195**, 186 (1999).
52. M. A. Moram, R. A. Oliver, M. J. Kappers, and C. J. Humphreys, Adv. Mater. , **21**, 3941 (2009).
53. A. Vilalta-Clemente et al., Phys Status Solidi A, **207**, 1105 (2010).
54. G. Cosendey, J-F Carlin, N. A. K. Kaufmann, R.Butte, and N.Grandjean Appl. Phys. Lett., **98**, 181111 (2011).
55. K. R. Wang et al., Appl. Phys. Lett, **96**, 231914 (2010).
56. C. Mauder et al., J. Cryst. Growth, **315**, 246 (2011).
57. C. Mauder et al., J. Cryst. Growth, **312**, 1823 (2010)].
58. C. Stampfl and C. G. Van de Walle, Phys. Rev. B, **57**, R15052 (1998).
59. L. H. Kuo, K. Kimura, A. Ohtake, S. Miwa, T. Yasuda, and T. Yao, J. Vac. Sci. Technol. B, **15**, 1241 (1997).
60. H. Hsu et al; Applied Physics Express, **4**, 035501 (2011).

61. M. Caliebe et al, Phys. Status Solidi B, 1 (2015)

62. Y. Gong et al, ECS Transactions, **66**, 151 (2015)

63. P. R. Edwards, L. K. Jagadamma, J. Bruckbauer, C. Liu, P. Shields, D. Allsopp, T. Wang and R. W. Martin, Microsc. Microanal. **18**, 1212 (2012).

64. P. R. Edwards and R. W. Martin, Semicond. Sci. Technol. **26**, 064005 (2011).

65. J. Bruckbauer et al., Appl. Phys. Lett. **98**, 141908 (2011).

66. F. Brunner, A. Mogilatenko, A. Knauer, M. Weyers, and J. T. Zettler, J. Appl. Phys. **112**, 033503, (2012).

67. H. Mansour et al, Scripta Materialia **84**, 11 (2014).

68. M. De Graef Microsc. Microanal. 18 (Suppl 2), 2012

69. Picard et al, Ultramicroscopy, **146**, 71 (2014).